IEEE Access
Multidisciplinary | Rapid Review | Open Access Journal

Received November 4, 2020, accepted November 28, 2020, date of publication December 17, 2020,
date of current version January 4, 2021.

Digital Object Identifier 10.1109/ACCESS.2020.3045605

Joint Deblurring and Denoising of THz Time-Domain Images

MARINA LJUBENOVIĆ[1], LINA ZHUANG[2], (Member, IEEE), JAN DE BEENHOUWER[3], AND JAN SIJBERS[3], (Associate Member, IEEE)

[1]Center for Cultural Heritage Technology, Italian Institute of Technology, 30175 Venice, Italy
[2]Department of Mathematics, Hong Kong Baptist University, Hong Kong
[3]imec-Vision Lab, Department of Physics, University of Antwerp, B-2610 Antwerp, Belgium

Corresponding author: Lina Zhuang (linazhuang@hkbu.edu.hk)

This work was supported in part by the Interuniversity Microelectronics Centre (IMEC)-B-budget Tera-Tomo project (project number 41672), in part by the Hong Kong Baptist University Start-up under Grant 21.4551.162562, and in part by the National Natural Science Foundation of China under Grant 42001287.

ABSTRACT Terahertz (THz) pulse/time-domain imaging attracted increased interest in recent years mostly due to its ability to extract dielectric properties of sample materials (i.e., absorption coefficient and the refraction index) from the amplitude and phase of each spectral component of the THz pulse. The resulting data from a THz time-domain system represents a 3-dimensional (3D) hyperspectral cube which contains several 2D images corresponding to different frequencies or bands. Due to a frequency-dependent non-zero THz beam waist, these 2D images are corrupted by blurring artifacts: a THz beam waist is wider on lower frequencies leading to more blurry corresponding 2D images. At higher frequencies, the beam waist is smaller resulting in sharper, but noisier images due to the decrease in the THz signal amplitude. The main focus of this work is the joint reduction of blur and noise from THz time-domain images. We propose two instances of a fast joint deblurring and denoising approach which is able to deal with THz time-domain images corrupted by different noise types and frequency-dependent blur. The experiments performed on synthetic and real THz time-domain images show that the proposed approach outperforms conventional 2D deblurring approaches and methods tailored to remote sensing hyperspectral images. To the best of our knowledge, this is the first time that a joint deblurring and denoising approach tailored to THz time-domain images is proposed taking into consideration band-dependent blur and different noise types.

INDEX TERMS Deblurring, denoising, THz imaging, THz-TDS.

I. INTRODUCTION

The terahertz (THz) region of the electromagnetic spectrum lies between 0.1 and 10 THz. In the past, this region, a so-called THz gap, which is located in between the microwave and the infrared band, was mostly neglected due to lack of inexpensive sources and detectors [1]. Nevertheless, in recent years, scientists from both electronics and optics pioneered many new THz techniques and systems enabling faster growth of the THz scientific field. This rapid growth is mostly due to immense progress in THz sources development [2] and the fact that the non-ionizing THz radiation, able to penetrate dialectic materials, is used in many applications (e.g., security [3], conservation of cultural heritage [4], and medicine [5]).

In this work, we are focused on a pulsed/time-domain THz imaging system in the transmission mode (the THz beam is transmitted through the sample). The THz time-domain spectroscopy (THz-TDS), a technique primarily developed for spectroscopy, has a huge impact on THz imaging [6]. A typical THz-TDS system contains a sub-picosecond pulsed laser followed by an antenna. The laser generates a sequence of pulses used to both generate and detect the THz radiation. A THz detector receives the THz radiation only for a short period of time, sampling the THz field at various delays. The structure of a THz-TDS system (i.e., a THz detector usually has a one (or few)-pixel structure [7], [8]) and the THz pulse generation procedure lead to measuring the THz electric field as a function of time, acquiring both amplitude and phase of detected pulses. For imaging applications, a THz pulse corresponding to a single pixel is transformed into a frequency domain by applying the Fourier transform: every pixel contains a complete THz time-domain waveform containing both the amplitude and the phase. Moreover, to be suitable for imaging, a THz-TDS system contains a set of focusing optics which increases the spatial resolution. The resulting data from a THz-TDS system represents a 3-dimensional (3D) hyperspectral cube which contains several two-dimensional (2D) images corresponding to different frequencies or bands.

The associate editor coordinating the review of this manuscript and approving it for publication was Chang-Hwan Son.

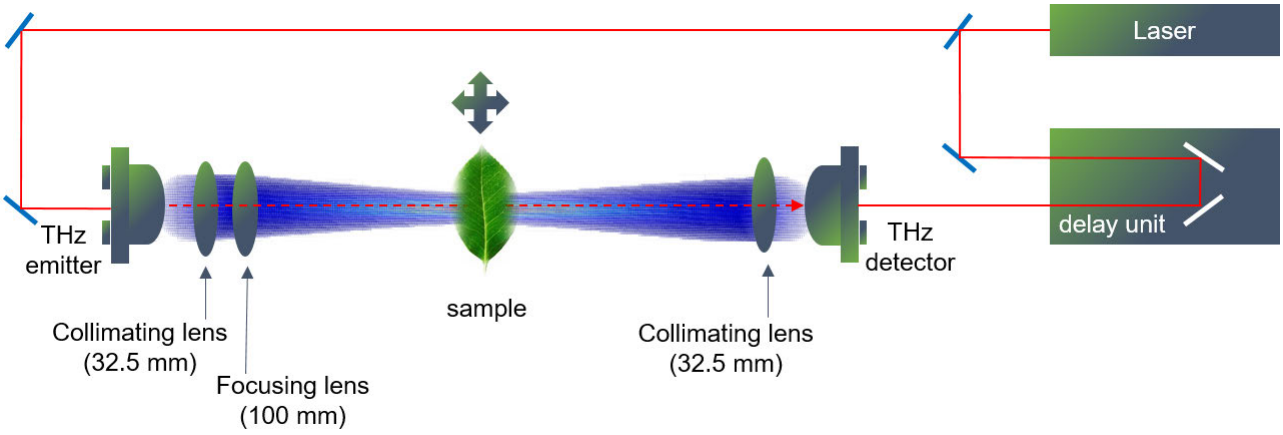

FIGURE 1. THz-TDS system in the transmittance mode.

Here, we are focused to exploiting imaging possibilities when working with THz time-domain hyperspectral (THz-HS) images.

There are many advantages of THz-TDS imaging. To name only a few: (i) THz-TDS has the ability to measure both the spectral amplitude, which is related to absorption of the sample, and phase, which relates to the sample thickness and density. The goal is to extract dielectric properties of the sample material (the absorption coefficient and the index of refraction) from the amplitude and phase of each spectral component in the THz pulse. (ii) The THz radiation generated by THz-TDS has a broad bandwidth (e.g., from 0.076 to 2 THz) used for spectroscopy as many materials have a unique fingerprint in the THz range [9]. iii) Additionally, we may choose to calculate a transmittance and phase-difference image by measuring a reference background by leaving the optical path open. An illustration of a simplified THz system in the transmission mode is shown in Figure 1.

The focal spot of the THz beam has a complex structure depending on a system design, focusing optics, and system frequencies. Namely, a THz beam waist (minimum beam radius) is wider at lower frequencies resulting in blurrier images. Contrary to that, at higher frequencies, we have a smaller beam waist and thus sharper images that are noisier since these images have lower amplitudes. Figure 2 shows three bands of THz-HS amplitude and phase images with the above-mentioned effects of blur and noise visible in the amplitude image. We assume that every pixel in the resulting image is blurred following a point-spread function (PSF) which represents an intersection of the THz beam on a fixed frequency in the sample position. Further, the THz-HS phase image (Figure 2 bottom row) shows different characteristics compared to the amplitude image: on some frequencies (e.g., 1.1368 THz), the structure and thickness of the leaf are more visible. The leaf was inserted in a black envelope prior to scanning and even if the envelope is made from a thin paper, we can see a clear difference in phase in the THz-HS phase image (the yellow stripe on the right-hand side).

The main focus of this work is jointly removing blur and noise from THz-HS amplitude and transmittance images. To jointly deblur and denoise THz-HS images, we exploit

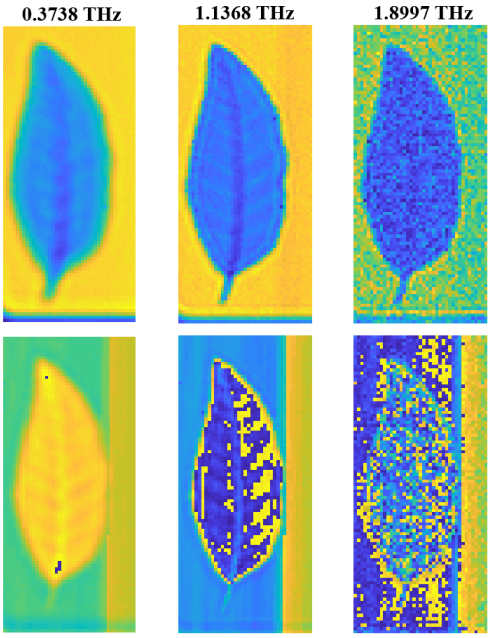

FIGURE 2. The THz-HS amplitude image (upper row) and phase image (bottom row) of a leaf at three different frequencies.

sparse HS image representations linked with their low-rank and self-similarity characteristics. Additionally, 2D images corresponding to one band are small in size (e.g., 41 × 61 pixels) compared to the PSF (e.g., 20 × 20 pixels) and not governed by similar statistics as in natural images. This makes the use of standard deblurring approaches to deblur THz-HS images difficult as these approaches are mostly tailored to natural or remote sensing images. Nevertheless, successful restoration of all bands of THz-HS images represents a huge impact on the non-destructive analysis of samples that contain multiple materials sometimes visible in different THz frequency ranges.

A. RELATED WORK

In recent years, several methods are proposed to deal with the above-mentioned blurring effects and increase the resolution of, mostly, 2D THz images. The authors of [10] tested several well-know super-resolution approaches applied

to THz images, such as projection on a convex set, iterative backprojection, Richardson-Lucy deblurring method [11], [12], and 2D wavelet decomposition reconstruction. These approaches are mainly developed for natural images and tested on THz images without additional adjustments, thus leading to limited performance. Other methods consider removing the blurring effects from THz images tailored to a specific application, such as THz computed tomography (CT) [13]. Here, the authors extend three well-known CT reconstruction approaches (i.e., back-projection of filtered projections, simultaneous algebraic reconstruction technique, and ordered subsets expectation-maximization) by introducing a convolution filter which corresponds to a THz beam. The method first introduces the acquisition simulator to estimate the impact of the THz beam profile on the projection sets. Furthermore, they remove the impact of the THz beam (i.e., convolution filter) by employing Wiener deconvolution [14]. In [15], the authors use a specially designed phantom to estimate the THz beam profile (i.e., PSF) related to a 2D image which corresponds to a fixed THz frequency and then employs Wiener deconvolution to remove its effect.

The recent progress in deep learning and neural networks (NN) inspired several papers for single THz image deblurring [16] and super-resolution [17], [18]. These methods use synthesized data to train NNs. One of the main limitations of NN-based methods is the requirement of a large number of THz images for training which is challenging to obtain. The one-pixel acquisition procedure is time-consuming: for instance, it takes around 2h for obtaining $50 \times 50 \times 263$ pixels image with the 0.2 mm acquisition step size. Moreover, raw THz images are corrupted by system-dependent blur and noise that is not possible to remove during the acquisition and reflection/refraction artifacts that are challenging to synthesize.

As previously explained, THz-HS images contain several bands corresponding to different frequencies (e.g., the leaf image dataset from Figure 2 has 263 bands). Therefore, next to the 2D deblurring methods applied to separate bands, it is natural to explore denoising, deblurring, and super-resolution approaches that consider bands of THz-HS images jointly. In the past, many methods have been developed to tackle these problems present in remote sensing HS images [19]–[22]. Low-rank and self-similarity characteristics of HS images inspired development of several state-of-the-art denoising methods [20], [21]. Moreover, some methods deal with HS image deblurring as part of other problems, such as segmentation [23] or unmixing [24]. Others are combining low-resolution HS images with high-resolution multispectral images to tackle the HS image super-resolution problem [25]. In [22], the authors proposed joint deblurring and denoising approach for HS images based on *principal component analysis* (PCA) and *total variation* (TV). They first employ dimensionality reduction using PCA followed by image restoration applied to a few HS image-bands. This approach combined with the methods exploiting low-rank and self-similarity characteristics inspired us to propose a joint denoising and deblurring method for THz-HS images.

Nevertheless, all the above mentioned HS image deblurring methods assume the same blurring effects over bands, an assumption that does not hold for THz-HS images. Here, the blurring effects, and therefore PSF, strongly depend on frequencies that are changing over bands. In order to tackle this challenge, we developed a method which contains several steps: i) we first assume that HS images live in a k-dimensional subspace, where k is much lower than the number of bands; ii) we project the original HS images into this subspace and perform denoising and deblurring only on the projected HS image; iii) finally, we reconstruct the sharp image by returning it into the original domain. This approach is a straightforward extension of the so-called FastHyDe method introduced in [21]. There are two main differences between FastHyDe and the proposed method: 1) we added a deblurring step and 2) we are considering different PSFs for different bands in the projected HS image.

B. CONTRIBUTIONS

Most of HS image denoising and deblurring methods are slow as they are usually reconstructing bands separately. In our work, we take full advantage of the high spectral correlation in the images to create a fast joint deblurring and denoising method:

1) We perform band by band deblurring and denoising only on the projected data which have k bands (e.g., in our implementation $k = 10$ which is much lower than original 263 bands), making the proposed approach significantly faster.

2) We are performing deblurring and denoising jointly: by projecting HS images into low-dimensional subspace, we remove a bulk of noise, making band by band deblurring much easier as noise is mostly removed.

3) We are considering different blur and noise over bands and therefore, we are able to tackle challenging real THz-HS images.

4) We are able to deal with three noise types: Gaussian i.i.d., Gaussian non-i.i.d., and Poissonian noise. We assume these noise types to make the proposed method more robust as THz-HS images in practice may be corrupted by noise from several sources [26]. With this assumption, we can restore both amplitude and transmittance THz-HS images.

5) We extended a deblurring method based on the well-known PCA and TV approaches, originally developed for remote sensing HS images [22] for tackling THz time-domain images.

To the best of our knowledge, this is the first time that a joint deblurring and denoising approach tailored to THz-HS images is proposed taking into consideration band-dependent blur and different noise types.

C. OUTLINE

In Section II, we briefly describe the THz beam modelling procedure. Section III reviews the FastHyDe method and introduces two instances of the proposed framework tailored

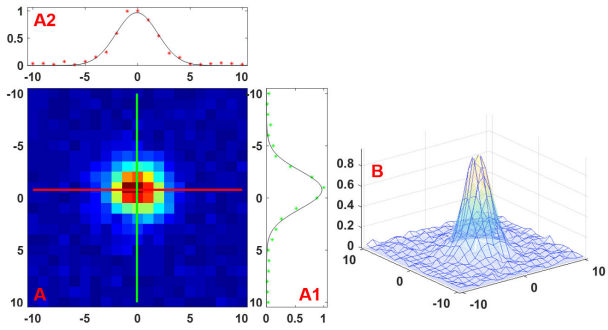

FIGURE 3. Measured THz beam profile: A - measured PSF on 0.76 THz with A1 and A2 representing 2D Gaussian distribution in two directions; B - fitted Gaussian distribution.

to three noise types. After presenting the proposed framework, in Sections IV and V we evaluate it on synthetic and real data respectively. Section VI concludes the manuscript and introduces the future work.

II. BEAM MODELLING

As previously explained, a THz beam has a non-zero beam waist and therefore introduces blurring effects in the resulting THz images. In order to remove these effects, in this work, we assume to know a THz beam shape and therefore, PSF in the position of a scanned sample. We follow the general beam modelling formulation where the THz beam is modelled as a Gaussian distribution parametrized by a beam waist and a frequency or wavelength [13]. Here, the radius of the beam at some position x from the beam waist w_0 is

$$w(x) = w_0\sqrt{1 + (\frac{x}{x_R})^2}, \tag{1}$$

where $x_R = \frac{\pi w_0^2}{\lambda}$ is the Rayleigh range with λ representing a wavelength. Moreover, the intensity distribution over cross-section in 3D is modelled as

$$I(x, y, z) = I_0(\frac{w_0}{w(x)})^2 \exp(\frac{-2(y^2 + z^2)}{w^2(x)}), \tag{2}$$

with I_0 as the beam intensity at the center of w_0 and y and z as distances from the beam axes in two directions.

To check the Gaussian beam assumption, we measured a THz beam and a beam profile at different frequencies. Measuring is done with a 3 mm aperture moved with a 1 mm step. Scanning square was set to 2cm × 2cm. Figure 3 shows a measured PSF on 0.76 THz (on the left side) and fitted Gaussian distribution (on the right side).

From (2), it is clear that several parameters define a THz beam: the wavelength (λ), the beam waist (w_0), and the intensity of the beam at w_0 (I_0). We can set these parameters to control a PSF model which represents an intersection of the 3D THz beam in a position of the scanned sample (see Figure 4).

III. FORMULATION AND PROPOSED METHOD

A. HS IMAGE DENOISING IN SUBSPACE DOMAIN

Assuming additive noise, a hyperspectral denoising problem is usually modelled as follows

$$\mathbf{Y} = \mathbf{X} + \mathbf{N}, \tag{3}$$

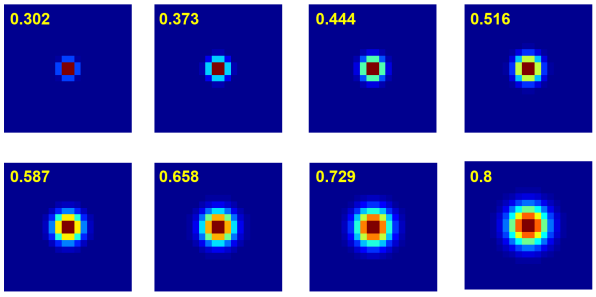

FIGURE 4. Influence of a THz beam waist on PSF: Examples of PSFs for 1 THz, $I_0 = 1$, and different w_0 in mm presented with the numbers in the upper-left corner.

where $\mathbf{Y} \in \mathbb{R}^{b\times n}$ represents an observed HS image with the rows containing b spectral bands. Every band is a vectorized image with n pixels corresponding to the transmittance or absorption coefficients. $\mathbf{X} \in \mathbb{R}^{b\times n}$ and $\mathbf{N} \in \mathbb{R}^{b\times n}$ represent an underlying clean HS image and noise, respectively.

Considering the high correlation between channels, we assume that the spectral vectors $\mathbf{x}_i$, for $i = 1, \ldots, n$, live in a k-dimensional subspace $\mathcal{S}_k$, with $k \ll b$. Following this assumption and defining $\mathbf{E} = [\mathbf{e}_1, \ldots, \mathbf{e}_k] \in \mathbb{R}^{b\times k}$ as a basis for $\mathcal{S}_k$, we may write

$$\mathbf{X} = \mathbf{E}\mathbf{A}, \tag{4}$$

where $\mathbf{A} \in \mathbb{R}^{k\times n}$ holds the representation coefficients of $\mathbf{X}$ in $\mathcal{S}_k$. The rows of $\mathbf{A}$ are herein called eigen-images. The above assumption is crucial as matrix $\mathbf{E}$ may be learned directly from $\mathbf{Y}$ by a *singular value decomposition* (SVD) of $\mathbf{Y}$ or subspace identification methods (e.g., HySime [20]).

The second assumption in [21] is self-similarity of eigen-images. Namely, eigen-images contain similar non-local image patches and therefore may be tackled by state-of-the-art denoising approaches based on a form of prior knowledge where the mentioned self-similarity is fully exploited (e.g., BM3D [27]).

Furthermore, the FastHyDe method is tailored to three noise types: Gaussian i.i.d, Gausian non-i.i.d, and Poissonian noise. Here, we will follow the same path starting from explaining the model with Gaussian i.i.d noise over all components of $\mathbf{N}$.

With $\mathbf{E}$ learned from the observed matrix $\mathbf{Y}$, the problem of denoising eigen-images is formulated as

$$\begin{aligned}\hat{\mathbf{A}} &\in \underset{\mathbf{A}}{\operatorname{argmin}} \frac{1}{2}||\mathbf{E}\mathbf{A} - \mathbf{Y}||_F^2 + \alpha\Phi(\mathbf{A}) \\ &= \underset{\mathbf{A}}{\operatorname{argmin}} \frac{1}{2}||\mathbf{A} - \mathbf{E}^T\mathbf{Y}||_F^2 + \alpha\Phi(\mathbf{A}),\end{aligned} \tag{5}$$

where $||\mathbf{M}||_F = \sqrt{\text{trace}(\mathbf{M}\mathbf{M}^T)}$ is the Frobenius norm of a matrix $\mathbf{M}$. The first term in (5) stands for the data fidelity and the second term represents a regularizer with the regularization parameter α which controls the relative contribution of the regularizer. In this work, a regularizer $\Phi(\cdot)$ depicts a prior knowledge that corresponds to self-similarity of image patches in the spatial domain.

Algorithm 1 HS Image Denoising in Subspace Domain (FastHyDe)

Input: Noisy HS image: $\mathbf{Y}$
Output: Denoised HS image: $\hat{\mathbf{X}}$
1: Learn the subspace $\mathbf{E}$ from $\mathbf{Y}$ using SVD or HySime [20].
2: Compute noisy eigen-images $\mathbf{E}^T\mathbf{Y}$.
3: Denoise eigen-images by a state-of-the-art denoiser one by one to get $\hat{\mathbf{A}}$.
4: Compute an estimate of the clean HS image: $\hat{\mathbf{X}} = \mathbf{E}\hat{\mathbf{A}}$.

We assume that eigen-images are decorrelated since the projection on subspace is a decorrelation transform. Thus the regularizer Φ can be decoupled as

$$\Phi(\mathbf{A}) = \sum_{i=1}^{k} \Phi_i(\mathbf{a}_i), \tag{6}$$

where $\mathbf{a}_i$ is the ith eigen-image, i.e., ith row of matrix $\mathbf{A}$ (more details can be find in [21]). Under this assumption, the equation (5) for one eigen-image $\mathbf{a}_i$ may be written as

$$\hat{\mathbf{a}}_i = \underset{\mathbf{a}_i}{\operatorname{argmin}} \frac{1}{2}||\mathbf{a}_i - \mathbf{e}_i^T\mathbf{Y}||_2^2 + \alpha\Phi_i(\mathbf{a}_i). \tag{7}$$

Recalling a definition of the proximity operator (PO) of a convex function f, computed at $\mathbf{v}$

$$\operatorname{prox}_f(\mathbf{v}) = \underset{\mathbf{x}}{\operatorname{argmin}} \frac{1}{2}||\mathbf{x} - \mathbf{v}||_F^2 + f(\mathbf{x}), \tag{8}$$

it is clear that (7) is the PO of function Φ_i at $\mathbf{e}_i^T\mathbf{Y}$.

Moreover, a PO can be seen as a denoising operator with the function f as a regularizer. This fact inspired a proposal of an image restoration framework, so-called plug-and-play [28], which promotes using state-of-the-art denoisers directly instead of finding an optimal regularizer and its PO. The FastHyDe method uses the same framework and replaces (7) with a state-of-the-art denoiser based on the non-local similarity property of image patches (e.g., BM3D [27]).

The FastHyDe method is summarized in Algorithm 1.

B. HS IMAGE DEBLURRING IN SUBSPACE DOMAIN

A HS image deblurring problem is usually modelled as

$$\mathbf{Y} = \mathbf{X}\mathbf{H} + \mathbf{N}, \tag{9}$$

where $\mathbf{H} \in \mathbb{R}^{n\times n}$ represents a blurring operator, which models a convolution of the HS image-bands and PSF. The above model assumes the same blurring operator over bands. If we want to remove blurring artefacts, the straightforward approach would be to perform band by band deblurring. Therefore, the deblurring problem for one band is modelled as

$$\mathbf{y}_i = \mathbf{H}\mathbf{x}_i + \mathbf{n}, \tag{10}$$

where $\mathbf{y}_i$, $\mathbf{x}_i$, and $\mathbf{n}$ represent an observed vectorized image of the ith band (ith row of $\mathbf{Y}$), a sharp image of the ith band, and noise respectively.

A common approach to tackle (10) is by solving the optimization problem

$$\hat{\mathbf{x}}_i = \underset{\mathbf{x}_i}{\operatorname{argmin}} \frac{1}{2}||\mathbf{y}_i - \mathbf{H}\mathbf{x}_i||_2^2 + \gamma_i g(\mathbf{x}_i), \tag{11}$$

where $g(\cdot)$ captures some form of regularizer or prior knowledge on $\mathbf{x}_i$ and γ_i its corresponding regularization parameter. One of the widely used regularization techniques for HS image deblurring is *total variation* (TV) [22] with

$$g(\mathbf{x}_i) = |\nabla\mathbf{x}_i|, \tag{12}$$

where ∇ represents the discrete gradient operator. TV is also known as a smoothing operator and it is widely used in image restoration problems for noise reduction. However, band by band TV-based deblurring of HS images is not fully utilizing cross-band correlation. Furthermore, the image reconstruction for each band and the parameter settings (i.e., γ_i needs to be set for every band separately) lead to a high computational cost.

One way to exploit cross-band correlation is by using the TV group sparsity regularization [29], where

$$g(\mathbf{x}_i) = \sum_{j=1}^{b} ||\nabla\mathbf{x}_j||_2, \tag{13}$$

where b represents a number of bands. The group sparsity combines the gradient coefficients of all spectral bands at the same spatial position. However, we still need to perform band by band deblurring and set a regularization parameter.

To overcome these two problems, in [22], the authors proposed an approach which contains several steps. They first perform *principal component analyses* (PCA) to decorrelate the HS image and then perform image deblurring only on the first p PCs by solving

$$\hat{\mathbf{x}}_i^{PC} = \underset{\mathbf{x}_i^{PC}}{\operatorname{argmin}} \frac{1}{2}||\mathbf{y}_i^{PC} - \mathbf{H}\mathbf{x}_i^{PC}||_2^2 + \gamma_1 \sum_{j=1}^{p} ||\nabla\mathbf{x}_j^{PC}||_2. \tag{14}$$

On the rest $b-p$ PCs they only perform denoising:

$$\hat{\mathbf{x}}_i^{PC} = \underset{\mathbf{x}_i^{PC}}{\operatorname{argmin}} \frac{1}{2}||\mathbf{y}_i^{PC} - \mathbf{x}_i^{PC}||_2^2 + \gamma_2 \sum_{j=p+1}^{b} ||\nabla\mathbf{x}_j^{PC}||_2. \tag{15}$$

γ_1 and γ_2 represent the regularization parameters for deblurring and denoising problems respectively. This approach is based on the assumption that most of the information is concentrated in the first several PCs while the rest contain a large amount of noise.

C. PROPOSED METHOD

The above-mentioned approach and the FastHyDe method inspired us to propose a new framework for HS image denoising and deblurring jointly. Namely, we extended the FastHyDe method to perform denoising and deblurring of THz-HS images. The main idea is to perform deblurring after subspace estimation, only on eigen-images, and not on the original HS image-bands. The main motivation behind this approach lies in the fact that after projection a bulk of noise is removed leading to better deblurring performance.

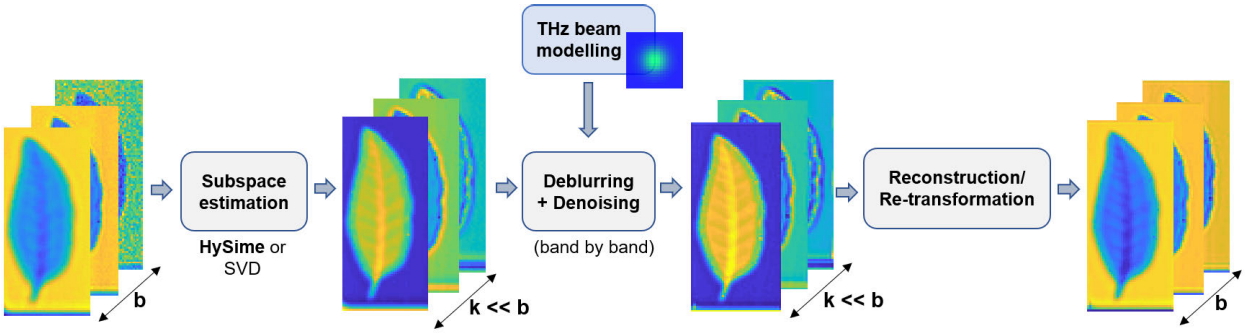

FIGURE 5. THz-HS joint deblurring and denoising pipeline illustration.

Similar to the FastHyDe approach, we start with subspace estimation from the observed image $\mathbf{Y}$ and compute eigen-images. The number of eigen-images is the same as the number of subspaces k which is significantly lower than the number of bands (in our implementation $k = 10$). Deblurring is performed by applying (11) on all k eigen-images followed by a state-of-the-art denoising. In implementation, PSFs related to eigen-images (i.e., $\mathbf{H}$ in (11)) are set by following the procedure introduced in Section II. To reduce the number of parameters for a THz beam modelling, some of them are fixed to pre-defined values (e.g., frequency = 1 THz and $I_0 = 1$) and w_0 is hand-tuned for the best results.

As explained in the introduction, one of the main characteristics of THz-HS images is that they are not corrupted equally over bands, namely: i) the beam waist depends on a frequency and therefore, the PSFs are different for different bands; ii) a noise level increases over bands. This fact leads to rewriting (10) as

$$\mathbf{y}_i = \mathbf{H}_i\mathbf{x}_i + \mathbf{n}_i, \tag{16}$$

where $\mathbf{H}_i$ represents a blurring operator for ith band and $\mathbf{n}_i$ denotes the corresponding noise components. From here, (11) becomes

$$\hat{\mathbf{x}}_i = \underset{\mathbf{x}_i}{\operatorname{argmin}} \frac{1}{2}||\mathbf{y}_i - \mathbf{H}_i\mathbf{x}_i||_2^2 + \gamma_i g(\mathbf{x}_i). \tag{17}$$

If deblurring is applied only on eigen-images, for the ith image we have

$$\tilde{\mathbf{a}}_i = \underset{\mathbf{a}_i}{\operatorname{argmin}} \frac{1}{2}||\mathbf{y}_i - \mathbf{H}_i\mathbf{E}\mathbf{a}_i||_2^2 + \gamma_i g(\mathbf{a}_i). \tag{18}$$

Similar as for FastHyDe, our approach contains several steps listed in Algorithm 2 and illustrated in Figure 5.

Deblurring of THz-HS images is a challenging task due to several reasons: 1) different bands are corrupted by different blurs; 2) in the spatial domain THz-HS images are small in size (e.g., 91 × 41 pixels) compared to the size of PSF (e.g., 20 × 20 pixels). The same is true for eigen-images and therefore the choice of a deblurring method has a great impact on the overall results.

To deblur eigen-images, we tested two well-known deblurring approaches for 2d images: the Richardson-Lucy method [11], [12] and TV-based deblurring [30]. We chose the Richardson-Lucy method as it is a simple approach where we are searching for a maximum likelihood solution without the use of any regularization. The majority of state-of-the-art deblurring methods use regularization or prior knowledge tailored to natural images. Therefore, due to the size and structure of THz images which is different from natural images, a strong regularizer will lead to poor deblurring results. Furthermore, the Richardson-Lucy method requires only one input parameter, namely, the number of iterations. Here, the number of iterations is fixed for all eigen-images. Moreover, we use TV-based deblurring as it is arguably the most common approach for hyperspectral image restoration and it can be used for different image types. We use the TV-based deblurring method from [30] with the following formulation:

$$\hat{\mathbf{x}}_i = \underset{\mathbf{x}_i}{\operatorname{argmin}} \frac{\mu}{2}||\mathbf{y}_i - \mathbf{H}_i\mathbf{x}_i||_2^2 + ||\mathbf{x}_i||_{TV}, \tag{19}$$

with

$$||\mathbf{x}_i||_{TV} = \sum_j \sqrt{\beta_x^2[D_x\mathbf{x}_i]_j^2 + \beta_y^2[D_y\mathbf{x}_i]_j^2}. \tag{20}$$

Operators D_x and D_y are the forward finite-difference operators along the horizontal and vertical directions and β_x and β_y are constants. $[\cdot]_j$ denotes the jth component of the vector $\mathbf{x}_i$ and μ the regularization parameter. We chose to use this approach as it uses an augmented Lagrangian optimization method which makes the method fast. Furthermore, the author provided a publicly available Matlab code.[1]

Algorithm 2 THz-HS Deblurring and Denoising

Input: Corrupted (blurry and noisy) THz images: $\mathbf{Y}$
Output: Deblurred and denoised THz images: $\hat{\mathbf{X}}$

1: Learn the subspace $\mathbf{E}$ from $\mathbf{Y}$ using SVD or HySime [20].
2: Compute corrupted eigen-images $\mathbf{E}^T\mathbf{Y}$.
3: Set PSFs for each eigen-image.
4: Deblur one by one eigen-images applying (18) to get $\tilde{\mathbf{A}}$.
5: Denoise $\tilde{\mathbf{A}}$ by a state-of-the-art denoiser one by one to get $\hat{\mathbf{A}}$.
6: Compute an estimate of the clean THz images: $\hat{\mathbf{X}} = \mathbf{E}\hat{\mathbf{A}}$.

[1] https://nl.mathworks.com/matlabcentral/fileexchange/43600-deconvtv-fast-algorithm-for-total-variation-deconvolution

D. ADDITIVE GAUSSIAN NON-I.I.D. NOISE

Assuming Gaussian i.i.d. noise, the spectral covariance $\mathbf{C}_\gamma = \sigma^2\mathbf{I}$, with σ representing a noise level and $\mathbf{I}$ the identity matrix. For non-i.i.d Gaussian noise, following the formulation from [21], we consider the observation model (9) with $\mathbf{N}$ as zero-mean, Gaussian, pixelwise independent with the spectral covariance $\mathbf{C}_\gamma = \mathbb{E}[\mathbf{n}_j\mathbf{n}_j^T]$, where $\mathbf{n}_j$ represents a column of $\mathbf{N}$. Note that $\mathbf{C}_\gamma$ can be estimated by hyperspectral noise estimation methods such as, HySime [20]. Converting non-i.i.d. scenario to i.i.d. one, leads to rewriting the observation data as

$$\bar{\mathbf{Y}} = \sqrt{\mathbf{C}_\gamma^{-1}}\mathbf{Y}, \tag{21}$$

where the noise covariance matrix is

$$\begin{aligned}\bar{\mathbf{C}}_\gamma &= \mathbb{E}[\sqrt{\mathbf{C}_\gamma^{-1}}n_j(\sqrt{\mathbf{C}_\gamma^{-1}}n_j)^T] \\ &= \mathbb{E}[\sqrt{\mathbf{C}_\gamma^{-1}}n_j n_j^T\sqrt{\mathbf{C}_\gamma^{-1}}^T] \\ &= \mathbb{E}[\sqrt{\mathbf{C}_\gamma^{-1}}\mathbf{C}_\gamma\sqrt{\mathbf{C}_\gamma^{-1}}^T] = \mathbf{I}.\end{aligned} \tag{22}$$

The above conversion is considered as an image preprocessing. The image $\bar{\mathbf{Y}}$ with i.i.d. noise now can be denoised and deblurred using the method we proposed in Subsection III-C. Finally, the clean HS image is estimated as $\hat{\mathbf{X}} = \sqrt{\mathbf{C}_\gamma}\bar{\mathbf{E}}\hat{\bar{\mathbf{A}}}$, where $\bar{\mathbf{E}}$ is learned from $\bar{\mathbf{Y}}$ and $\hat{\bar{\mathbf{A}}}$ represent estimated eigen-images of $\bar{\mathbf{Y}}$.

E. POISONNIAN NOISE

When assuming Poissonian noise, we may apply the Anscombe transformation to $\mathbf{Y}$ [31]:

$$\bar{\mathbf{Y}} = 2\sqrt{\mathbf{Y}} + \frac{3}{8}. \tag{23}$$

The Anscombe transformation converts Poissonian noise to an approximation of Gaussian noise. From here, to formulate a deblurring problem, we are following the steps explained in Subsection III-D.

IV. EVALUATION WITH SYNTHETIC DATA

To evaluate the proposed method, we created 200 synthetic hyperspectral images. When creating synthetic data, we took into consideration several aspects: 1) size of the synthetic images should be close to the size of real (acquired) images (e.g., $61 \times 41 \times 263$ pixels); 2) PSFs are different over bands and controlled by setting w_0 and λ in (1) and (2); 3) we are considering different noise types and levels in order to synthesize both amplitude and transmittance images; 4) intensity change over bands is taken into account. Next, we will explain in more details how we synthesized images.

A. CREATING SYNTHETIC DATA

As briefly explained in the introduction, when using THz-TDS system in the transmittance mode, we may have four output images: amplitude, phase, transmittance, and phase-difference. We aim to deblur both amplitude and transmittance images as they have a different role in some applications, such as detection of water content in plants [32].

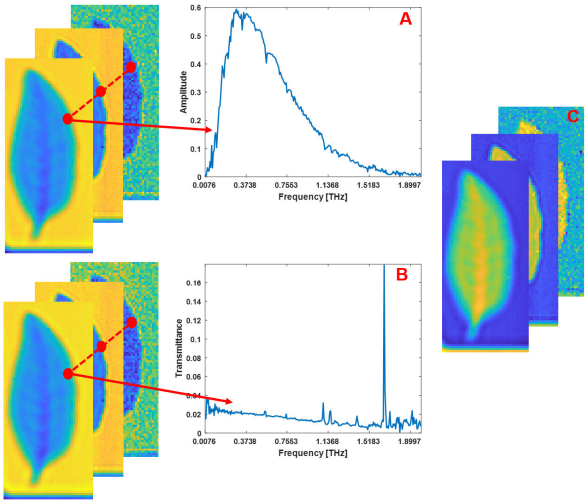

FIGURE 6. Spectral responses of (A) THz-HS amplitude image, (B) THz-HS transmittance image, and (C) their pixel-by-pixel difference.

We apply the same approach to these two types of THz images with different noise type assumption (more details in Section V). To see a difference between amplitude and transmittance images, we may look at their spectral responses and pixel-by-pixel difference shown in Figure 6. We plotted the intensity of the pixel at the same position in the spatial domain in both images over all bands (whole frequency range). From here, it is clear that the spectral responses have a different distribution over bands that we should take into account when creating synthetic images. Note that the peaks visible in the spectral response of the transmittance image is probably due to water vapour as the THz radiation is highly absorbed by water [33].

The synthetic images are created by following three main steps: 1) extract spectral responses from a real image or use a THz spectral library such the one provided by NICT THz Project[2]; 2) combine spectral responses with a grayscale or an RGB image which contains simple-shaped objects; 3) add blur and noise to all bands. The whole procedure is illustrated in Figure 7. The synthetic datasets are created by considering two noise types:

- The first set contains 100 test images corrupted by Gaussian i.i.d. noise ($\mathbf{n}_i \sim \mathcal{N}(\mathbf{0}, \sigma^2\mathbf{I})$) with the maximum noise level for the band corresponding to the highest frequency $\sigma = 0.1$. The band corresponding to the lowest frequency is a considered noise free.
- The second set contains 100 test images corrupted by Poissonian noise with $\mathbf{y}_i \sim \mathcal{P}(\alpha\mathbf{x}_i)$, where $\mathcal{P}(\mathbf{m})$ represents a vector of independent random variables with the Poisson distribution whose parameters are defined as $\mathbf{m} = [m_i]$. The parameter α is chosen such that $\text{SNR} = \alpha\frac{(\sum_i m_i^2)}{\sum_i m_i}$. SNR is set from 80 dB for the first band to 25 dB for the last one.

[2]https://webbook.nist.gov/chemistry/thz-ir/

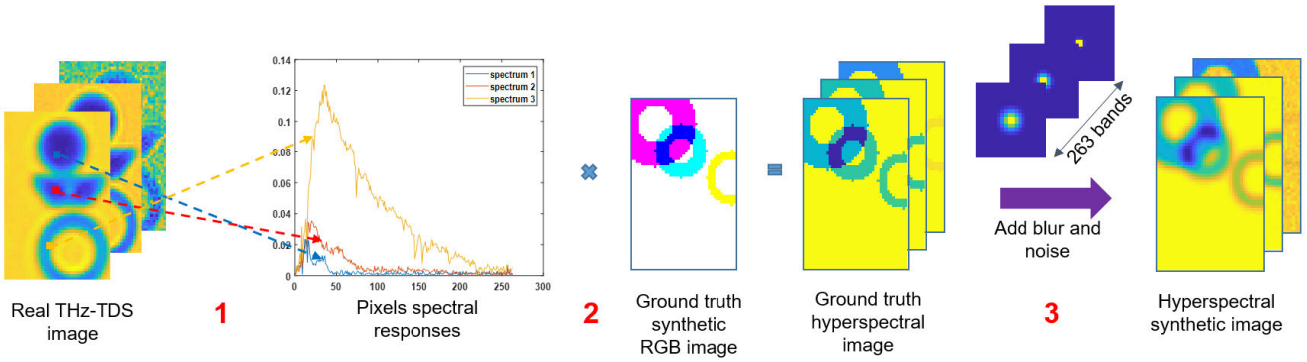

FIGURE 7. Creating THz-HS synthetic data.

B. EXPERIMENTS WITH SYNTHETIC DATA

To evaluate the proposed framework, as a measurement metrics, we use well-known *peak signal-to-noise ratio* (PSNR), *structural similarity index* (SSIM), and *improvement on signal-to-noise ratio* (ISNR) defined as

$$\text{ISNR} = 10\log_{10}\frac{||\mathbf{x}-\mathbf{y}||_2^2}{||\mathbf{x}-\hat{\mathbf{x}}||_2^2}, \tag{24}$$

where $\mathbf{x}$, $\mathbf{y}$, and $\hat{\mathbf{x}}$ represent the ground truth image, the observed image, and the estimated image of one band respectively.

We tested the proposed joint deblurring and denoising framework with the deblurring step performed with two 2D deblurring approaches: Richardson-Lucy method (R-L) and TV-based deblurring (TV). Additionally, we tested these two image deblurring methods by applying them to separate HS image-bands. Before performing band by band deblurring, HS images were denoised with the FastHyDe method. This is an important preprocessing step as noise may influence the deblurring results significantly. Additionally, the obtained results are compared with the PCA-based method introduced in [22] (PCA + TV).

To set the blurring filters corresponding to eigen-images when testing the proposed method we: i) hand-tuned a PSF-related parameter, beam waist (w_0) and ii) fixed the frequency on a pre-defined value.

Figure 8 shows mean ISNR values over all bands for 100 test images from the second set (i.e., images corrupted by Poissonian noise). The proposed framework with TV-based deblurring step shows the best results in terms of mean ISNR. Some ISNR values for the R-L method applied to HS image-bands separately are below zero which means that the PSNR values of the estimated image are below the PSNR of the corresponding blurred image.

Furthermore, Figure 9 shows the visual results obtained on two synthetic THz-HS images selected from the first set, one containing simple-shaped squared objects (left) and the other with several objects which combined give the more complex-shape structure (right). We show the estimated images corresponding to four bands (i.e., bands 44, 70, 150, and 263). The first row presents the ground truth bands and the second row shows corrupted (blurred and noisy) ones. Results of

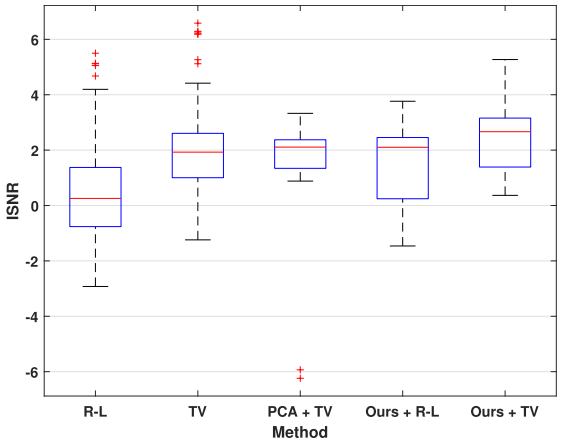

FIGURE 8. Comparison of mean ISNR over bands of 100 synthetic images from the second set. R-L: Denoising + Band by band deblurring with the R-L method; TV: Denoising + Band by band deblurring with TV-based method; PCA + TV: PCA method with the TV-based deblurring; Ours + R-L: The proposed framework with the R-L step; Ours + TV: The proposed framework with the TV-based step.

band by band deblurring with R-L and TV are shown in rows three and four, respectively (note that the HS images are denoised before deblurring). We can see that the estimated image obtained by R-L contains ringing artefacts. Additionally, results obtained with both band by band deblurring methods suffer from cyclic boundary artifacts. The results obtained with the PCA-based method are presented in the fifth row. Finally, the results of the proposed framework are presented in rows six (Ours + R-L) and seven (Ours + TV). The PCA-based method gives comparable results to the proposed one with more constant output over bands compared to the band by band deblurring.

Finally, Figure 10 shows PSNR, SSIM, and ISNR values over bands for TV-based band by band deblurring and the proposed framework with the TV-based step. The experiments are performed on the image from the right-hand side of Figure 9 (as previously, the THz-HS image is denoised before 2D deblurring). We chose to compare these two approaches due to two reasons: i) on lower bands, visually the results are comparable and the difference in the performance can only be fully appreciated when analysing ISNR values. ii) The proposed method (Ours + TV), arguably shows the

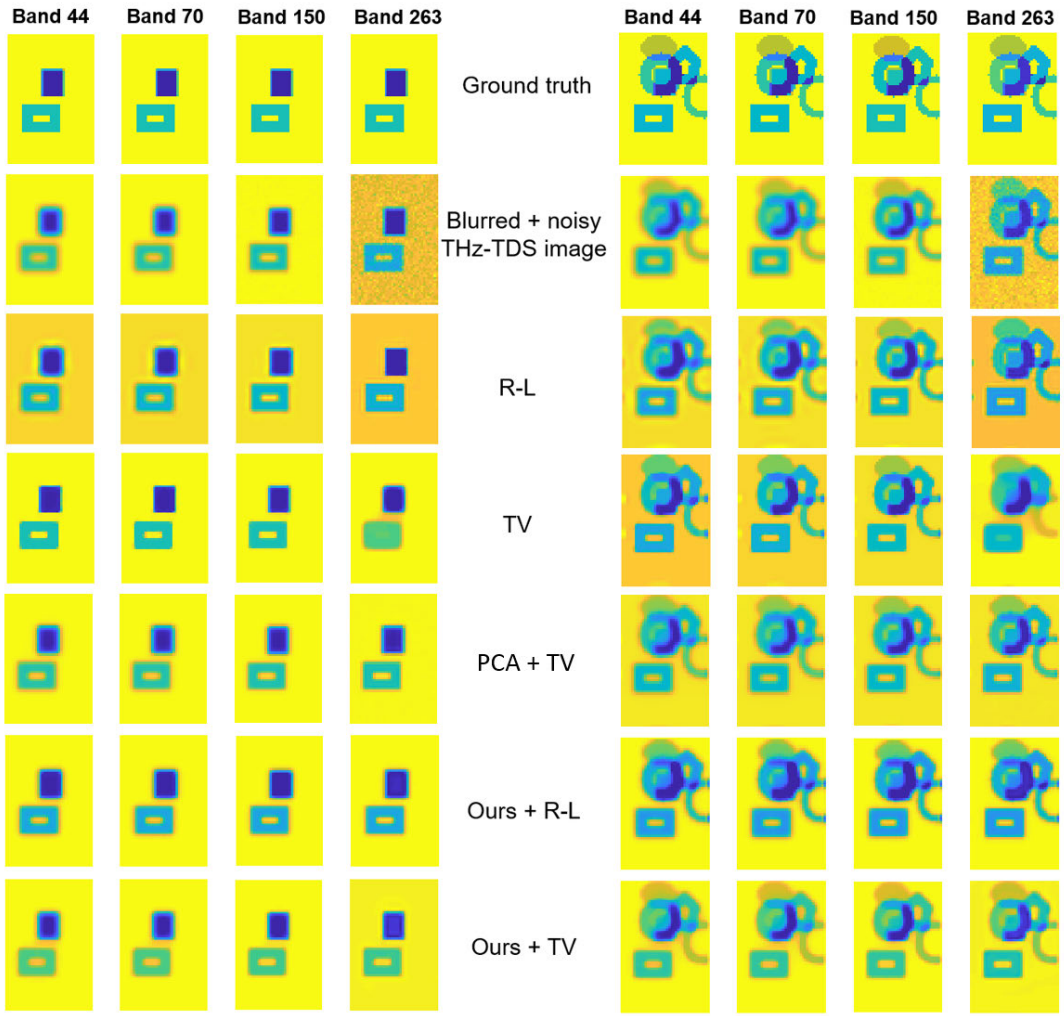

FIGURE 9. Comparison of visual results performed on synthetic THz-HS images. R-L: Denoising + Band by band deblurring with the R-L method; TV: Denoising + Band by band deblurring with TV-based method; PCA + TV: PCA method with the TV-based deblurring; Ours + R-L: The proposed framework with the R-L step; Ours + TV: The proposed framework with TV-based step.

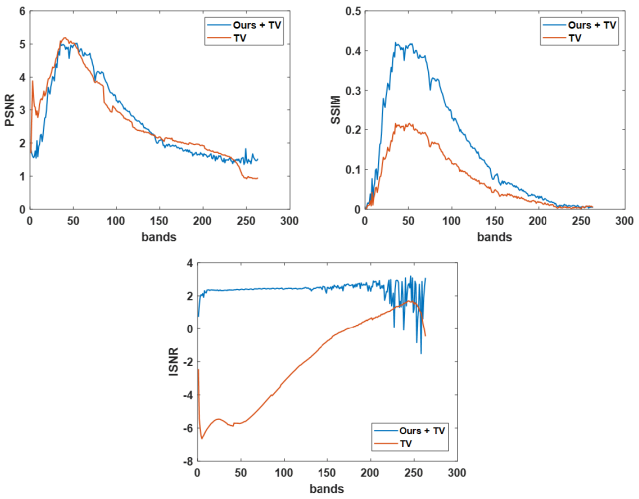

FIGURE 10. Values of PSNR, SSIM, and ISNR over bands (synthetic image from Figure 9 - right): The proposed framework with TV-based step vs. band by band TV deblurring.

best performance when tested on synthetic THz images. PSNR values are comparable for both methods. Nevertheless, the proposed method significantly outperforms band by band deblurring in terms of SSIM and ISNR.

V. EVALUATION WITH REAL DATA

The real data are acquired using a non-commercial THz-TDS system with the configuration illustrated in Figure 1. The frequency step is set to 7.6 GHz starting from 0 to 2 THz (263 frequencies in total). The system gives four hyperspectral images as explained above: amplitude, transmittance, phase, and phase difference. We acquired three sets of images. The first set contains a leaf (spatial dimension 91×41 pixels) and the second contains three simple objects with known dimensions: plastic plate, knife blade, and metal ring (image spatial dimension is 61×41 pixels). The metal ring has an inner diameter of 20 mm and an outer diameter of 25.5 mm. The knife's short edge is 15 mm, the long edge is 29 mm, and it has a centre hole of 3.5 mm. The plastic plate has a diameter of 18 mm. The third set of images contains a chocolate bar with whole hazelnuts (Leche Con Avellanas Enteras Melk Hele Hazelnoot by Ritter Sport). The leaf and the simple-shaped objects are placed in a black non-transparent

TABLE 1. Running time of the proposed framework compared to the PCA-based method and methods for 2d band by band image deblurring. Columns: 1) Tested methods; 2) Amplitude image with spatial size 61 × 41 pixels; 3) Transmittance image with spatial size 61 × 41 pixels; 4) Amplitude image with spatial size 91 × 41 pixels; 5) Transmittance image with spatial size 91 × 41 pixels.

time [seconds]	HS image 61x41 amplitude	HS image 61x41 transmittance	HS image 91x41 amplitude	HS image 91x41 transmittance
R-L	81.673	82.415	82.732	84.518
TV	108.152	108.744	110.274	111.67
PCA + TV	7.654	7.197	8.225	8.464
Ours + R-L	**3.456**	**3.356**	**3.552**	**3.434**
Ours + TV	4.418	4.422	4.616	4.661

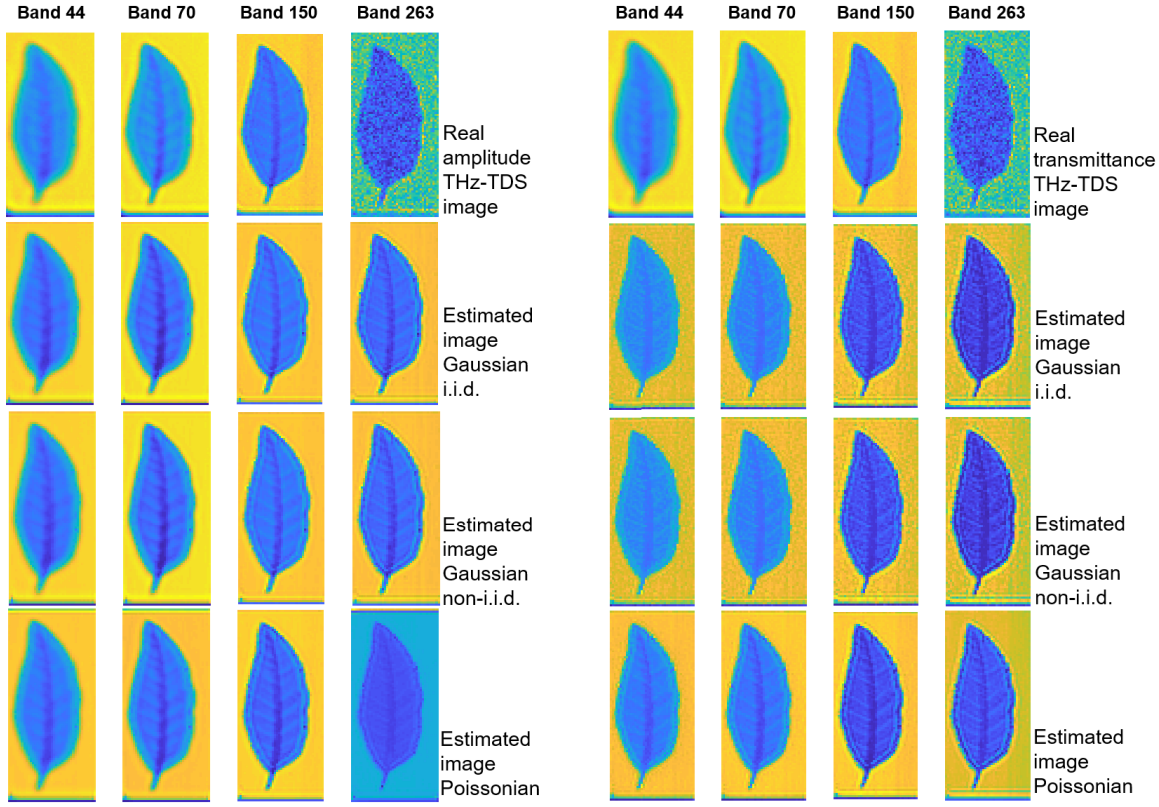

FIGURE 11. THz-HS amplitude (left) and transmittance (right) images estimates for different noise types. Columns: 44, 70, 150, and 263 band respectively; Rows: Real THz time-domain image, Gaussian i.i.d., Gaussian non-i.i.d., and Poissonian noise.

envelope during scanning. The chocolate is scanned inside a wrap.

Similar to the experiments with synthetic data, the PSFs assumed for eigen-images are hand-tuned by setting the appropriate parameters, a frequency and a beam waist.

First, we compare the running times of the proposed framework with the Richardson-Lucy approach (Ours + R-L) and TV-based approach (Ours + TV) as a 2D deblurring step, with the running times of band by band-based deblurring and the PCA-based method. The results are presented in Table 1. It is clear that the proposed framework significantly speeds up the deblurring process compared to the band by band approaches. Compared to the PCA-based deblurring, the proposed method halve the processing time. Deblurring is slightly faster if we use the R-L step compared to the TV-based step as we limit the number of iterations (here we perform only four iterations). We tested both amplitude and transmittance images. For amplitude images, we assume Gaussian i.i.d. noise and for transmittance images, we assume Poissonian noise. By assuming Poissonian noise, we employ the Anscombe transformation which may slightly increase the processing time.

Next, we tested how the choice of a noise type influence the results. Figure 11 shows four bands of estimated amplitude and transmittance images with the assumption of three noise types: Gaussian i.i.d., Gaussian non-i.i.d., and Poissonian noise. To estimate the images, we used the proposed framework with the R-L step. The results imply that we should assume Gaussian noise if we deal with amplitude THz-HS images and Poissonian noise in case of transmittance images.

Furthermore, Figure 12 shows the influence of two 2D-based deblurring methods introduced as a step of the proposed framework on the estimated amplitude and transmittance images. As explained previously, in the case of an amplitude image we assume Gaussian i.i.d. noise and for the

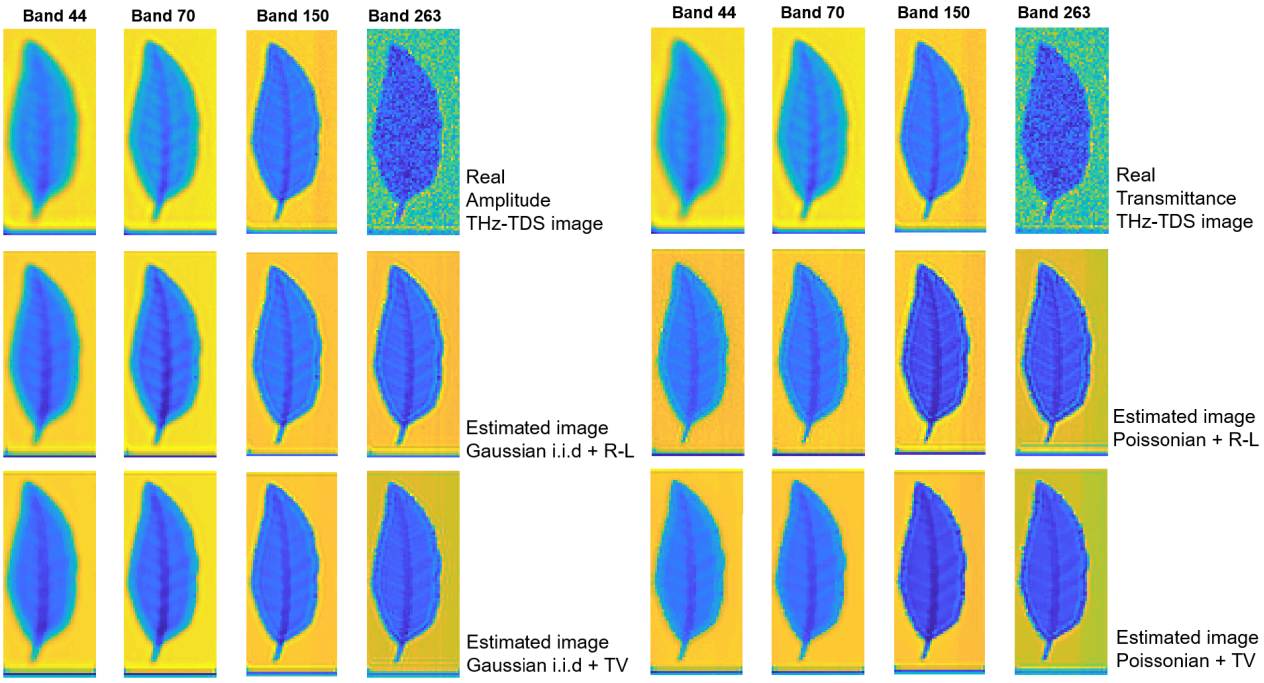

FIGURE 12. THz-HS amplitude (left) and transmittance (right) image estimates for different choice of inner deblurring method. Columns: 44, 70, 150, and 263 band respectively; Rows: Real THz time-domain image, results of the proposed method with R-L deblurring, and results of the proposed method with TV deblurring.

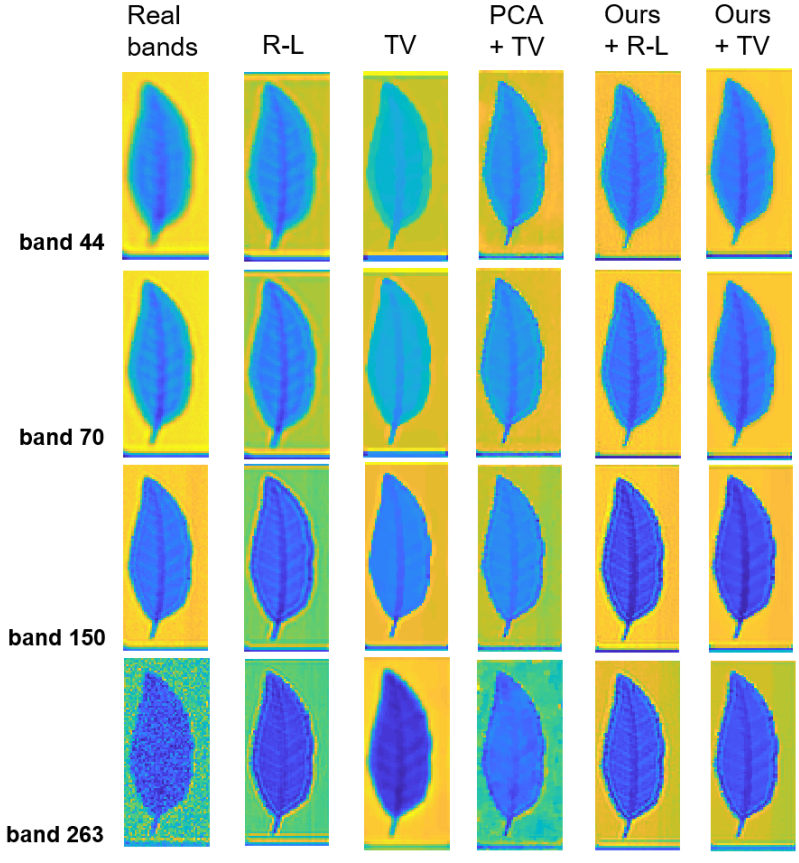

FIGURE 13. Our methods compared to 2D band-by-band deblurring and the method based on PCA tested on the leaf transmittance image.

transmittance image, we assume Poissonian noise. For both, amplitude and transmittance images, the results show that when the TV-based method is employed we lose some details, i.e., the image is over-smoothed.

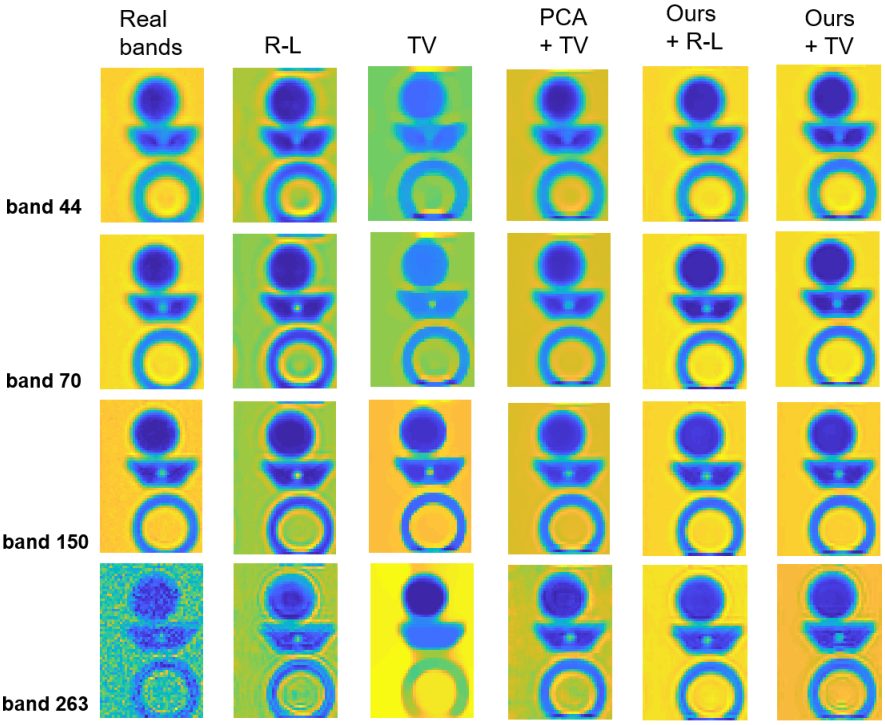

FIGURE 14. Our methods compared to 2d band-by-band deblurring and the method based on PCA tested on the amplitude image that contains simple objects.

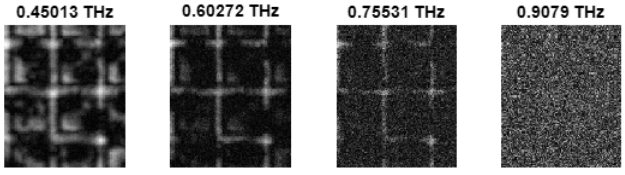

FIGURE 15. Bands of the chocolate bar sample.

Next, we compared the performance of the R-L and TV methods applied band by band and as a step of the proposed framework. Additionally, the PCA-based deblurring is tested. Figures 13 and 14 show the four bands of the estimated transmittance THz-HS image containing a leaf and the amplitude THz-HS image containing simple-shaped objects respectively. The results of the proposed framework show more constant performance over bands compared to the band by band deblurring. The images estimated with the R-L method show the ringing artifacts and poor deblurring results on lower bands. The TV-based method over-smooths the resulting images. As previously explained, before performing band by band deblurring we denoise the images with the FastHyDe method. Similarly as TV-based band by band deblurring, PCA + TV over-smooths small details and introduces additional artifacts in higher bands when dealing with the transmittance image. Note that the PCA-based approach is implemented in its original form with the blurring kernel fixed and equal for all PC bands. The halo artifact, especially visible in bands corresponding to higher frequencies, most likely arose due to reflection losses (the ring is made of metal and therefore highly reflecting in the THz domain).

Figure 15 shows four selected bands of the transmittance image obtained on the chocolate bar sample. A chocolate

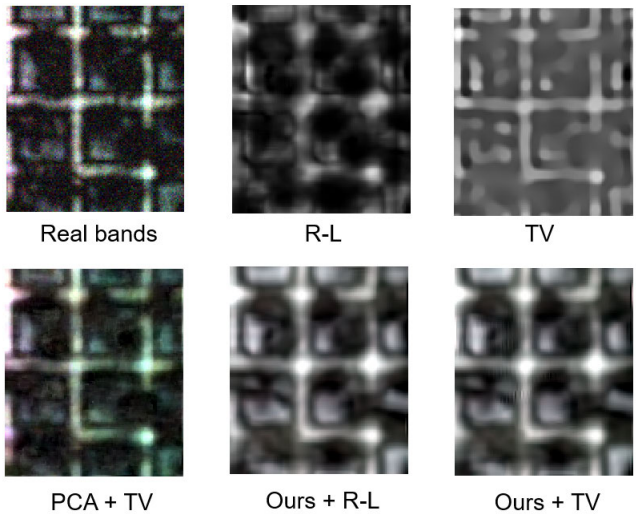

FIGURE 16. Our methods compared to 2d band-by-band deblurring and the method based on PCA tested on the transmittance image that contains chocolate sample.

bar contains two main parts, chocolate and hazelnuts, and it is highly absorbing leading do the low amplitude of the transmitted signal and thus, strong noise in the resulting image (note that 0.9079 THz corresponds to band 120).

Figure 16 shows the results obtained on the chocolate with hazelnuts sample. The results are presented as false RGB images created by combining three bands (i.e., 70, 71, and 72) corresponding to 0.526, 0.534, and 0.542 THz respectively. As previously, the HS image is denoised prior to performing band by band deblurring (i.e., R-L and TV methods). The results of the 2D-based methods show limited performance:

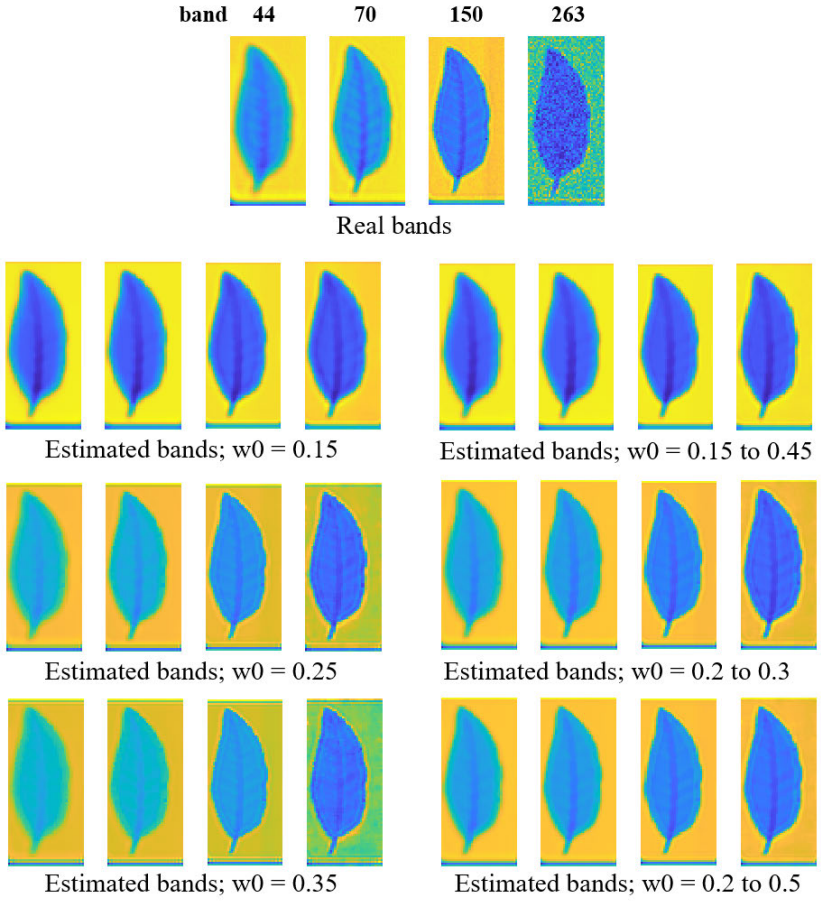

FIGURE 17. PCA-based method: setting the blurring kernel parameters. The experiments performed on the leaf amplitude image.

the R-L method generates severe ringing artifacts and the TV-based method over-smooths image borders. The PCA + TV method (with PSFs fixed over bands) shows promising results with keeping pixels intensity levels close to the raw data. When applying this method, the border of hazelnuts remains blurred and thus, less distinguishable. The proposed methods (i.e., Ours + R-L and Ours + TV) remove the noise fully and slightly sharpen the image inner-structure leading to better identification of different parts of the sample (e.g., chocolate and hazelnuts).

Finally, we adapted the PCA-based approach, originally developed for remote sensing HS images, to THz-HS images by varying the PSFs corresponding to different PCs. The results with the fixed and varied PSFs are presented in Figure 17. Here, the frequency is set to 1 THz and we only vary the beam waist (w_0).

VI. CONCLUSION

In this work, we propose a joint deblurring and denoising method tailored to THz (amplitude and transmittance) time-domain images. The proposed method is inspired by well-known restoration methods for remote sensing HS images and adjusted to time-domain THz images. The experiments performed on synthetic and real data show that the proposed method outperforms existing ones in several aspects: i) computational cost, ii) robustness to different noise types, and iii) overall deblurring and denoising performance assessed visually and by applying three measurement metrics, e.g., PSNR, SSIM, and ISNR.

Moreover, we explore the PCA-based method, originally developed for remote sensing HS images, and extended it for tackling THz-HS images. To the best of our knowledge, this is the first time that THz-HS images are jointly deblurred and denoised by taking into consideration variations over bands.

The limitation of the proposed approach is reflected in the fact that the parameters of PSFs corresponding to eigen-images are hand-tuned. These is due to the fact that these PSFs are not a linear combination of the original ones (i.e., blurring kernels corresponding to the original bands) and therefore, can not be easily calculated from the measured blurring kernels. The calculation of the PSFs is covered by our current work. Our future work will tend to overcome the need for manual parameter settings (e.g., THz beam waist and parameters related to the 2D deblurring step). Moreover, we are working on a new procedure for THz data synthesization that can improve evaluation of model-based methods and open a path for developing novel approaches based on deep neural networks.

ACKNOWLEDGMENT

The authors would like to thank Pavel Paramonov from imec-Vision Lab for fruitful discussions. They would also like to thank Bert Gyselinckx and Lei Zhang from imec USA and Sachin Kasture, Roelof Jansen, and Xavier Rottenberg from imec for discussions and help with data acquisition.

REFERENCES

[1] W. L. Chan, J. Deibel, and D. M. Mittleman, "Imaging with terahertz radiation," *Rep. Progr. Phys.*, vol. 70, no. 8, pp. 1325–1379, Jul. 2007.

[2] J. P. Guillet, B. Recur, L. Frederique, B. Bousquet, L. Canioni, I. Manek-Hönninger, P. Desbarats, and P. Mounaix, "Review of terahertz tomography techniques," *J. Infr., Millim., Terahertz Waves*, vol. 35, no. 4, pp. 382–411, Apr. 2014. [Online]. Available: https://hal.archives-ouvertes.fr/hal-00968839

[3] M. C. Kemp, P. F. Taday, B. E. Cole, J. A. Cluff, A. J. Fitzgerald, and W. R. Tribe, "Security applications of terahertz technology," in *Terahertz for Military and Security Applications* (International Society for Optics and Photonics), vol. 5070, R. J. Hwu and D. L. Woolard, Eds. Orlando, FL, USA: SPIE, 2003, pp. 44–52, doi: 10.1117/12.500491.

[4] A. Cosentino, "Terahertz and cultural heritage science: Examination of art and archaeology," *Technologies*, vol. 4, no. 1, p. 6, Feb. 2016. [Online]. Available: https://www.mdpi.com/2227-7080/4/1/6

[5] E. Pickwell-MacPherson and V. P. Wallace, "Terahertz pulsed imaging—A potential medical imaging modality?" *Photodiagnosis Photodynamic Therapy*, vol. 6, no. 2, pp. 128–134, Jun. 2009.

[6] B. B. Hu and M. C. Nuss, "Imaging with terahertz waves," *Opt. Lett.*, vol. 20, no. 16, pp. 1716–1718, Apr. 1995. [Online]. Available: http://ol.osa.org/abstract.cfm?URI=ol-20-16-1716

[7] S. Nadar, H. Videlier, D. Coquillat, F. Teppe, M. Sakowicz, N. Dyakonova, W. Knap, D. Seliuta, I. Kašalynas, and G. Valušis, "Room temperature imaging at 1.63 and 2.54 THz with field effect transistor detectors," *J. Appl. Phys.*, vol. 108, no. 5, Sep. 2010, Art. no. 054508.

[8] M. Burger, J. Föcke, L. Nickel, P. Jung, and S. Augustin, *Reconstruction Methods THz Single-Pixel Imaging*. Cham, Switzerland: Springer, 2019, pp. 263–290.

[9] J. B. Baxter and G. W. Guglietta, "Terahertz Spectroscopy," *Anal. Chem.*, vol. 83, no. 12, pp. 4342–4368, 2011.

[10] L.-M. Xu, W.-H. Fan, and J. Liu, "High-resolution reconstruction for terahertz imaging," *Appl. Opt.*, vol. 53, no. 33, p. 7891, 2014.

[11] W. H. Richardson, "Bayesian-based iterative method of image restoration," *J. Opt. Soc. Amer.*, vol. 62, no. 1, pp. 55–59, Jan. 1972. [Online]. Available: http://www.osapublishing.org/abstract.cfm?URI=josa-62-1-55

[12] L. B. Lucy, "An iterative technique for the rectification of observed distributions," *Astronomical J.*, vol. 79, no. 6, pp. 745–754, 1974.

[13] B. Recur, J. P. Guillet, I. Manek-Hönninger, J. C. Delagnes, W. Benharbone, P. Desbarats, J. P. Domenger, L. Canioni, and P. Mounaix, "Propagation Beam Consideration for 3D THz Computed Tomography," *Opt. Exp.*, vol. 20, no. 6, pp. 5817–5829, 2012. [Online]. Available: http://www.opticsexpress.org/abstract.cfm?URI=oe-20-6-5817

[14] A. P. Dhawan, R. M. Rangayyan, and R. Gordon, "Image restoration by Wiener deconvolution in limited-view computed tomography," *Appl. Opt.*, vol. 24, no. 23, p. 4013, Dec. 1985.

[15] D. C. Popescu and A. D. Hellicar, "Point spread function estimation for a terahertz imaging system," *EURASIP J. Adv. Signal Process.*, vol. 2010, no. 1, Dec. 2010, Art. no. 575817, doi: 10.1155/2010/575817.

[16] M. Ljubenović, S. Bazrafkan, J. De Beenhouwer, and J. Sijbers, "CNN-based deblurring of terahertz images," in *Proc. 15th Int. Joint Conf. Comput. Vis., Imag. Comput. Graph. Theory Appl.*, 2020, pp. 323–330.

[17] Z. Li, Z. Cen, and X. Li, "A terahertz image super-resolution reconstruction algorithm based on the deep convolutional neural network," in *Optical Sensing and Imaging Technology and Applications*, vol. 10462, Y. Jiang, H. Gong, W. Chen, and J. Li, Eds. Bellingham, WA, USA: SPIE, 2017, pp. 353–361, doi: 10.1117/12.2283469.

[18] Z. Long, T. Wang, C. You, Z. Yang, K. Wang, and J. Liu, "Terahertz image super-resolution based on a deep convolutional neural network," *Appl. Opt.*, vol. 58, no. 10, pp. 2731–2735, Apr. 2019. [Online]. Available: http://ao.osa.org/abstract.cfm?URI=ao-58-10-2731

[19] A. Plaza, J. A. Benediktsson, J. W. Boardman, J. Brazile, L. Bruzzone, G. Camps-Valls, J. Chanussot, M. Fauvel, P. Gamba, A. Gualtieri, M. Marconcini, J. C. Tilton, and G. Trianni, "Recent advances in techniques for hyperspectral image processing," *Remote Sens. Environ.*, vol. 113, pp. S110–S122, Dec. 2009. [Online]. Available: http://www.sciencedirect.com/science/article/pii/S0034425709000807

[20] J. M. P. Nascimento and J. M. Bioucas-Dias, "Hyperspectral Signal Subspace Estimation," in *Proc. IEEE Int. Geosci. Remote Sens. Symp.*, Jul. 2007, pp. 3225–3228.

[21] L. Zhuang and J. M. Bioucas-Dias, "Fast hyperspectral image denoising and inpainting based on low-rank and sparse representations," *IEEE J. Sel. Topics Appl. Earth Observ. Remote Sens.*, vol. 11, no. 3, pp. 730–742, Mar. 2018.

[22] W. Liao, B. Goossens, J. Aelterman, H. Q. Luong, A. Pizurica, N. Wouters, W. Saeys, and W. Philips, "Hyperspectral image deblurring with PCA and total variation," in *Proc. 5th Workshop Hyperspectral Image Signal Process., Evol. Remote Sens.*, Jun. 2013. p. 4.

[23] F. Li, M. K. Ng, and R. J. Plemmons, "Coupled segmentation and denoising/deblurring models for hyperspectral material identification," *Numer. Linear Algebra with Appl.*, vol. 19, no. 1, pp. 153–173, Jan. 2012. [Online]. Available: https://onlinelibrary.wiley.com/doi/abs/10.1002/nla.750

[24] X.-L. Zhao, F. Wang, T.-Z. Huang, M. K. Ng, and R. J. Plemmons, "Deblurring and sparse unmixing for hyperspectral images," *IEEE Trans. Geosci. Remote Sens.*, vol. 51, no. 7, pp. 4045–4058, Jul. 2013.

[25] R. Dian, S. Li, L. Fang, and J. Bioucas-Dias, "Hyperspectral image super-resolution via local low-rank and sparse representations," in *Proc. IEEE Int. Geosci. Remote Sens. Symp.*, Jul. 2018, pp. 4003–4006.

[26] L. Duvillaret, F. Garet, and J.-L. Coutaz, "Influence of noise on the characterization of materials by terahertz time-domain spectroscopy," *JOSA B*, vol. 17, pp. 452–461, 03 2000.

[27] K. Dabov, A. Foi, V. Katkovnik, and K. Egiazarian, "Image denoising by sparse 3-D transform-domain collaborative filtering," *IEEE Trans. Image Process.*, vol. 16, no. 8, pp. 2080–2095, Dec. 2007.

[28] S. V. Venkatakrishnan, C. A. Bouman, and B. Wohlberg, "Plug-and-play priors for model based reconstruction," in *Proc. IEEE Global Conf. Signal Inf. Process.*, Dec. 2013, pp. 945–948.

[29] A. Majumdar and R. K. Ward, "Compressed sensing of color images," *Signal Process.*, vol. 90, no. 12, pp. 3122–3127, Dec. 2010.

[30] S. H. Chan, R. Khoshabeh, K. B. Gibson, P. E. Gill, and T. Q. Nguyen, "An augmented Lagrangian method for total variation video restoration," *IEEE Trans. Image Process.*, vol. 20, no. 11, pp. 3097–3111, Nov. 2011, doi: 10.1109/TIP.2011.2158229.

[31] F. J. Anscombe, "The transformation of poisson, binomial and negative-binomial data," *Biometrika*, vol. 35, nos. 3–4, pp. 246–254, 1948. [Online]. Available: http://www.jstor.org/stable/2332343

[32] P. Nie, F. Qu, L. Lin, T. Dong, Y. He, Y. Shao, and Y. Zhang, "Detection of water content in rapeseed leaves using terahertz spectroscopy," *Sensors*, vol. 17, no. 12, p. 2830, Dec. 2017.

[33] Z. Song, S. Yan, Z. Zang, Y. Fu, D. Wei, H.-L. Cui, and P. Lai, "Temporal and spatial variability of water status in plant leaves by terahertz imaging," *IEEE Trans. Terahertz Sci. Technol.*, vol. 8, no. 5, pp. 520–527, Sep. 2018.

MARINA LJUBENOVIĆ received the bachelor's and master's degrees in telecommunications and signal processing from the Faculty of Technical Sciences, University of Novi Sad, Serbia, and the Ph.D. degree in electrotechnics and computer sciences from the Institute Superior Tecnico, University of Lisbon. During her Ph.D., she was a part of the Marie Curie Innovative Training Network (MacSeNet) and she was employed as an Early Stage Researcher at the Institute for Telecommunications in Lisbon. After her Ph.D. studies, she was a Post-Doctoral Researcher at Vision Lab, University of Antwerp, Belgium. She is currently a Post-Doctoral Researcher with the IIT Center for Cultural Heritage Technology, Venice, Italy. Her research interests include model-based and machine learning-based methods for super-resolution, denoising, and deblurring of document, hyperspectral, and terahertz images.

LINA ZHUANG (Member, IEEE) received the bachelor's degrees in geographic information system and in economics from South China Normal University, Guangzhou, China, in 2012, the M.S. degree in cartography and geography information systems from the Institute of Remote Sensing and Digital Earth, Chinese Academy of Sciences, Beijing, China, in 2015, and the Ph.D. degree in electrical and computer engineering from the Instituto Superior Técnico, Universidade de Lisboa, Lisbon, Portugal. She is currently a Research Assistant Professor with the Department of Mathematics, Hong Kong Baptist University, Hong Kong. Her research interests include hyperspectral image denoising, inpainting, superresolution, and compressive sensing.

JAN DE BEENHOUWER received the M.Sc. degree in computer science engineering from KU Leuven, Belgium, in 2003, and the Ph.D. degree in biomedical engineering from Ghent University, Belgium, in 2008, where he was a Post-Doctoral Fellow for two years, prior to joining the imec-Vision Lab, University of Antwerp, Belgium, where he was a research leader of the ASTRA Tomography Group. He is currently an Assistant Professor with the University of Antwerp. His main interest is in image reconstruction with a focus on X-ray computed tomography and electron tomography.

JAN SIJBERS (Associate Member, IEEE) received the M.Sc. degree in physics and the Ph.D. degree in sciences/physics from the University of Antwerp, Belgium, in 1993 and 1998, respectively. He was a Post-Doctoral Fellow with the Fund for Scientific Research from 2002 to 2008, jointly with the University of Antwerp and the Delft University of Technology, The Netherlands. He is currently a Full Professor with the University of Antwerp. He is also the Head of the imec-Vision Lab and the Co-Founder of IcoMetrix and Deltaray. His main interest is in biomedical image reconstruction, processing, and analysis, with a focus on diffusion MRI processing and iterative reconstruction for computed tomography. He is currently a Senior Area Editor of the IEEE TRANSACTIONS ON IMAGE PROCESSING and an Associate Editor of the IEEE TRANSACTIONS ON MEDICAL IMAGING.